

## Fe<sub>2</sub>O<sub>3</sub> Nanoparticle Seed Catalysts Enhance Cyclability on Deep (Dis)charge in Aprotic Li-O<sub>2</sub> Batteries

Li, Zhaolong; Ganapathy, Swapna; Xu, Yaolin; Zhu, Quanyao; Chen, Wen; Kochetkov, Ivan; George, Chandra; Nazar, Linda F.; Wagemaker, Marnix

**DOI**

[10.1002/aenm.201703513](https://doi.org/10.1002/aenm.201703513)

**Publication date**

2018

**Document Version**

Final published version

**Published in**

Advanced Energy Materials

**Citation (APA)**

Li, Z., Ganapathy, S., Xu, Y., Zhu, Q., Chen, W., Kochetkov, I., George, C., Nazar, L. F., & Wagemaker, M. (2018). Fe<sub>2</sub>O<sub>3</sub> Nanoparticle Seed Catalysts Enhance Cyclability on Deep (Dis)charge in Aprotic Li-O<sub>2</sub> Batteries. *Advanced Energy Materials*, (1703513), 1-9. <https://doi.org/10.1002/aenm.201703513>

**Important note**

To cite this publication, please use the final published version (if applicable).  
Please check the document version above.

**Copyright**

Other than for strictly personal use, it is not permitted to download, forward or distribute the text or part of it, without the consent of the author(s) and/or copyright holder(s), unless the work is under an open content license such as Creative Commons.

**Takedown policy**

Please contact us and provide details if you believe this document breaches copyrights.  
We will remove access to the work immediately and investigate your claim.

# Fe<sub>2</sub>O<sub>3</sub> Nanoparticle Seed Catalysts Enhance Cyclability on Deep (Dis)charge in Aprotic Li–O<sub>2</sub> Batteries

Zhaolong Li, Swapna Ganapathy, Yaolin Xu, Quanyao Zhu, Wen Chen, Ivan Kochetkov, Chandramohan George, Linda F. Nazar, and Marnix Wagemaker\*

Although the high energy density of Li–O<sub>2</sub> chemistry is promising for vehicle electrification, the poor stability and parasitic reactions associated with carbon-based cathodes and the insulating nature of discharge products limit their rechargeability and energy density. In this study, a cathode material consisting of  $\alpha$ -Fe<sub>2</sub>O<sub>3</sub> nanoseeds and carbon nanotubes (CNT) is presented, which achieves excellent cycling stability on deep (dis)charge with high capacity. The initial capacity of Fe<sub>2</sub>O<sub>3</sub>/CNT electrode reaches 805 mA h g<sup>-1</sup> (0.7 mA h cm<sup>-2</sup>) at 0.2 mA cm<sup>-2</sup>, while maintaining a capacity of 1098 mA h g<sup>-1</sup> (0.95 mA h cm<sup>-2</sup>) after 50 cycles. The operando structural, spectroscopic, and morphological analysis on the evolution of Li<sub>2</sub>O<sub>2</sub> indicates preferential Li<sub>2</sub>O<sub>2</sub> growth on the Fe<sub>2</sub>O<sub>3</sub>. The similar d-spacing of the (100) Li<sub>2</sub>O<sub>2</sub> and (104) Fe<sub>2</sub>O<sub>3</sub> planes suggest that the latter epitaxially induces Li<sub>2</sub>O<sub>2</sub> nucleation. This results in larger Li<sub>2</sub>O<sub>2</sub> primary crystallites and smaller secondary particles compared to that deposited on CNT, which enhances the reversibility of the Li<sub>2</sub>O<sub>2</sub> formation and leads to more stable interfaces within the electrode. The mechanistic insights into dual-functional materials that act both as stable host substrates and promote redox reactions in Li–O<sub>2</sub> batteries represent new opportunities for optimizing the discharge product morphology, leading to high cycling stability and coulombic efficiency.

decomposition (oxygen evolution reaction, OER) of Li<sub>2</sub>O<sub>2</sub> according to the reaction  $2\text{Li} + \text{O}_2 \xrightleftharpoons[\text{charge}]{\text{discharge}} \text{Li}_2\text{O}_2$ .<sup>[1]</sup> Therefore, the performance of this battery is determined by the reversibility of Li<sub>2</sub>O<sub>2</sub> redox and the electrolyte stability.<sup>[1]</sup> The morphology and mechanism of Li<sub>2</sub>O<sub>2</sub> deposition depends on the relative stability of the intermediate LiO<sub>2</sub> product in the electrolyte and the time scale of the Li<sub>2</sub>O<sub>2</sub> formation on the cathode surface. While LiO<sub>2</sub> stability is determined by the stabilization of the Li<sup>+</sup> both through the solvation strength of the electrolyte (quantified by the donor number (DN)) and the association strength of the counter anion,<sup>[5–7]</sup> the time scale determines to what extent the intermediate LiO<sub>2</sub> species are solvated.<sup>[8]</sup> In an intermediate DN electrolyte, such as tetraethylene glycol dimethyl ether (TEGDME), the nucleation and growth of toroidal Li<sub>2</sub>O<sub>2</sub> particles were proposed to occur via the solution dismutase mechanism at low current rates, whereas at fast

## 1. Introduction

Rechargeable aprotic Li–air or Li–O<sub>2</sub> batteries have great potential to enable energy-hungry applications, owing to their extremely high theoretical specific energy density.<sup>[1–4]</sup> In typical aprotic Li–O<sub>2</sub> batteries, the (dis)charge process proceeds via the formation (oxygen reduction reaction, ORR) and

rates quasi-amorphous thin films were observed on electrode surface.<sup>[8]</sup> Porous carbon based materials have been extensively explored as O<sub>2</sub> gas diffusion electrodes because of their high surface area, low weight, and low cost. Unfortunately, the discharge product Li<sub>2</sub>O<sub>2</sub> reacts with carbon and the electrolyte at high potentials that characterize the OER process, and forms byproducts that clog the electrode pores, resulting in capacity fading and poor cycling stability.<sup>[9,10]</sup> Significant efforts have been expended in mitigating these side reactions by employing several combinations of noble metals (Au, Ru/RuO<sub>2</sub>, and Pt),<sup>[11–21]</sup> transition metal oxides (MnO<sub>2</sub>, Co/CoO/Co<sub>3</sub>O<sub>4</sub>, NiO, and TiO<sub>2</sub>),<sup>[22–33]</sup> and metal-related compounds,<sup>[34–40]</sup> both as catalysts and conductive matrices to improve the energy efficiency and cycle life of the Li–O<sub>2</sub> batteries.

Most often the reported cycling performance of Li–O<sub>2</sub> systems is based on capacity-limited cycling, rather than the preferred potential-limited cycling where the full electrode capacity is utilized. Capacity-limited cycling performance of batteries makes it difficult to quantify if improved cycling stability can be attributed to the specific role of electrode or to the continuous consumption of new active sites on the electrode surface is delivered. To date, the only electrode systems that have displayed improved reversible Li<sub>2</sub>O<sub>2</sub> formation and decomposition during potential limited cycling in aprotic Li–O<sub>2</sub> batteries are porous gold,<sup>[14]</sup> metallic RuO<sub>2</sub>,<sup>[41,42]</sup> the metallic porous

Z. Li, Dr. S. Ganapathy, Y. Xu, Dr. C. George, Prof. M. Wagemaker

Department of Radiation Science and Technology

Delft University of Technology

Mekelweg 15, 2629JB Delft, The Netherlands

E-mail: m.wagemaker@tudelft.nl

Prof. Q. Zhu, Prof. W. Chen

State Key Laboratory of Advanced Technology for

Materials Synthesis and Processing

School of Materials Science and Engineering

Wuhan University of Technology

Wuhan 430070, P. R. China

I. Kochetkov, Prof. L. F. Nazar

Department of Chemistry and the Waterloo Institute for Nanotechnology

University of Waterloo

Waterloo, Ontario N2L 3G1, Canada

The ORCID identification number(s) for the author(s) of this article can be found under <https://doi.org/10.1002/aenm.201703513>.

DOI: 10.1002/aenm.201703513

Magnéli phase  $\text{Ti}_4\text{O}_7$ ,<sup>[43]</sup> and  $\text{TiC}$ .<sup>[37]</sup> However, Ru and Au are heavy elements that limit their gravimetric energy density, and their high cost makes them unlikely candidates for practical Li–O<sub>2</sub> batteries. TiC-based cathodes also exhibit good capacity retention but have a relatively low gravimetric capacity (about 350 mA h g<sup>-1</sup> in dimethyl sulfoxide (DMSO) electrolyte and 520 mA h g<sup>-1</sup> in TEGDME electrolyte),<sup>[37]</sup> and the same holds true for  $\text{Ti}_4\text{O}_7$  electrodes.<sup>[43]</sup> Alternatively, iron and iron oxide are both low-cost and abundant, and carbon-supported iron-based catalysts<sup>[44–47]</sup> have been studied as O<sub>2</sub> diffusion electrodes for Li–O<sub>2</sub> batteries. Although iron oxide electrodes have been shown to exhibit lower overpotential, a higher capacity and better cycling performance compared to carbon electrodes upon capacity-limited cycling, full (dis)charge (with potential limited cycling) has not been reported to date, which is in fact a key figure-of-merit for these batteries.

Hematite  $\text{Fe}_2\text{O}_3$  is known as a O<sub>2</sub> reduction catalyst in aqueous media<sup>[48,49]</sup> and as an O<sub>2</sub> adsorption material.<sup>[50]</sup> While it is ostensibly a wide band gap semiconductor, the presence of structural defects leads to significant electronic conductivity.<sup>[50]</sup> Shimizu et al.<sup>[48]</sup> and Sun et al.<sup>[49]</sup> found that via its catalytic activity,  $\text{Fe}_2\text{O}_3$  could alter the ORR reaction pathway from a 2e<sup>-</sup> to a 4e<sup>-</sup> process in aqueous media. Gurlo et al.<sup>[50]</sup> have reported that oxygen could preferentially adsorb on the  $\alpha$ - $\text{Fe}_2\text{O}_3$  surface, and Zhang et al.<sup>[33]</sup> found that  $\text{Co}_3\text{O}_4$  acted as crystal seed by preferential oxygen adsorption, facilitating the formation of  $\text{Li}_2\text{O}_2$  film and particles. Motivated by these observations, our work reported here demonstrates that oxygen cathodes prepared by a combination of nanosized  $\text{Fe}_2\text{O}_3$  seed crystallites with carbon nanotubes (CNT) exhibit an impressive cycle stability and large capacity when cycled in a large potential cutoff window of 2.0–4.5 V. The initial specific capacity of the  $\text{Fe}_2\text{O}_3/\text{CNT}$  electrode reaches about 805 mA h g<sup>-1</sup> (0.70 mA h cm<sup>-2</sup>), and it maintains a reversible capacity of  $\approx 1098$  mA h g<sup>-1</sup> (0.95 mA h cm<sup>-2</sup>) after 50 cycles at a current density of 0.2 mA cm<sup>-2</sup>. We propose that the similar (104)  $\text{Fe}_2\text{O}_3$  and (100)  $\text{Li}_2\text{O}_2$  lattice plane d-spacing induces epitaxial growth of  $\text{Li}_2\text{O}_2$  on the  $\text{Fe}_2\text{O}_3$  surface. The epitaxial growth enhances the nucleation of  $\text{Li}_2\text{O}_2$  which enhances its crystallinity, and suppresses amorphous  $\text{Li}_2\text{O}_2$  formation which leads to passivation. This epitaxial growth of  $\text{Li}_2\text{O}_2$  on  $\text{Fe}_2\text{O}_3$  nanoparticles results in oriented and smaller secondary  $\text{Li}_2\text{O}_2$  particles, which are responsible for more facile decomposition upon oxidation. The preferential formation of  $\text{Li}_2\text{O}_2$  on  $\text{Fe}_2\text{O}_3$  and the facile decomposition are proposed to be responsible for the significantly improved reversible  $\text{Li}_2\text{O}_2$  formation and decomposition leading to the observed high capacity retention on deep (dis)charge.

## 2. Results and discussion

### 2.1. Electrochemical Performance

The use of  $\text{Fe}_2\text{O}_3$  nanoseed crystals in the gas diffusion cathode was also motivated by our previous study, where hexagonal NiO nanocrystals ( $a = b = 2.972 \pm 0.001$  Å,  $c = 7.158 \pm 0.001$  Å) were found to induce equiaxial growth of  $\text{Li}_2\text{O}_2$  ( $a = b = 3.142 \pm 0.005$  Å,  $c = 7.650 \pm 0.005$  Å) due to an approximate match of their *a*- and *b*-lattice parameters.<sup>[30]</sup> The lattice parameters of the  $\alpha$ - $\text{Fe}_2\text{O}_3$

( $a = b = 5.5035$  Å and  $c = 13.74$  Å) are distinct from  $\text{Li}_2\text{O}_2$ ; however, the interplanar spacing of its (104) (2.70 Å) and (110) (2.52 Å) planes are approximately equal to the (100) (2.72 Å) and (101) (2.56 Å) planes of  $\text{Li}_2\text{O}_2$  (Figure S1, Supporting Information). The CNTs play an important role in forming an interpenetrating porous network structure that facilitates access of O<sub>2</sub>, and they also provide electronic conductivity across electrodes and support the  $\text{Fe}_2\text{O}_3$  catalyst.

Figure 1 displays the galvanostatic (dis)charge cycle performance of Li–O<sub>2</sub> batteries with CNT and  $\text{Fe}_2\text{O}_3/\text{CNT}$  cathodes by employing a potential cutoff at different (dis)charge current densities. The Brunauer-Emmett-Teller (BET) surface of the cast  $\text{Fe}_2\text{O}_3/\text{CNT}$  cathodes (75/25 wt%) is smaller, 8.47 m<sup>2</sup> g<sup>-1</sup>, compared to that of the CNT powder (150–200 m<sup>2</sup> g<sup>-1</sup>). Therefore, the effective electrochemical surface area of  $\text{Fe}_2\text{O}_3/\text{CNT}$  electrodes must be significantly smaller compared to the CNT cathodes. This implies that when applying the same current density, based on the geometrical surface of the cathodes, the local current density should be expected to be larger for the  $\text{Fe}_2\text{O}_3/\text{CNT}$  cathodes. The cycling stability of the CNT cathode is relatively poor (Figure 1a–c), and after 30 cycles the specific discharge capacity decreases drastically at current densities of 0.1 and 0.2 mA h cm<sup>-2</sup>. Under the same cycling conditions, despite the fact that the local current density should be larger, the  $\text{Fe}_2\text{O}_3/\text{CNT}$  cathode shows significantly better cycling stability and coulombic efficiency, as shown in Figure 1d–f. The reversible specific capacity on deep (dis)charge of the  $\text{Fe}_2\text{O}_3/\text{CNT}$  electrode reaches 1295 mA h g<sup>-1</sup> after 50 cycles at a current density of 0.1 mA cm<sup>-2</sup> (based on the total mass of the  $\text{Fe}_2\text{O}_3$  and CNT), which is larger than the first discharge capacity (951 mA h g<sup>-1</sup>). Also at a current density of 0.2 mA cm<sup>-2</sup>, the initial specific discharge capacity of the  $\text{Fe}_2\text{O}_3/\text{CNT}$  cathode is 805 mA h g<sup>-1</sup>, and it maintains a capacity of 1098 mA h g<sup>-1</sup> after 50 cycles. The incremental capacity over cycling is most likely the result of continuous activation of the  $\text{Fe}_2\text{O}_3$  surface due to the gradual impregnation of the electrolyte into the porous structure of CNT and  $\text{Fe}_2\text{O}_3$  nanoparticles, which activates more reaction surface over time.<sup>[41]</sup>

Interestingly, after the first cycle the specific capacity of the  $\text{Fe}_2\text{O}_3/\text{CNT}$  cathode (normalized using geometric surface of the electrode) is larger than that of the CNT cathode (Figure S2, Supporting Information). Again we note that the electrochemical surface area of the  $\text{Fe}_2\text{O}_3$  electrodes is expected to be smaller based on the smaller  $\text{Fe}_2\text{O}_3$  surface area compared to that of CNT. The initial discharge capacity of the  $\text{Fe}_2\text{O}_3/\text{CNT}$  cathode is 0.6 and 0.7 mA h cm<sup>-2</sup>, and 0.95 and 1.05 mA h cm<sup>-2</sup> for the CNT cathode at current densities of 0.1 and 0.2 mA cm<sup>-2</sup>, respectively (Figure S2, Supporting Information). However, after 30 deep (dis)charge cycles, the capacities of the CNT electrode dramatically drop to almost zero. On the contrary, the capacity of the  $\text{Fe}_2\text{O}_3/\text{CNT}$  electrode increases to 0.85 and 0.95 mA h cm<sup>-2</sup> after 50 deep (dis)charge cycles at current densities of 0.1 and 0.2 mA cm<sup>-2</sup>, respectively. The results indicate that the  $\text{Fe}_2\text{O}_3/\text{CNT}$  cathode surface is more active toward ORR compared to the CNT cathode, hence triggering the formation of more  $\text{Li}_2\text{O}_2$ . The charge overpotential of the  $\text{Fe}_2\text{O}_3/\text{CNT}$  electrode is 200 mV lower than that of the CNT cathode (Figure S3, Supporting Information), which was also observed in other studies.<sup>[44,45]</sup>

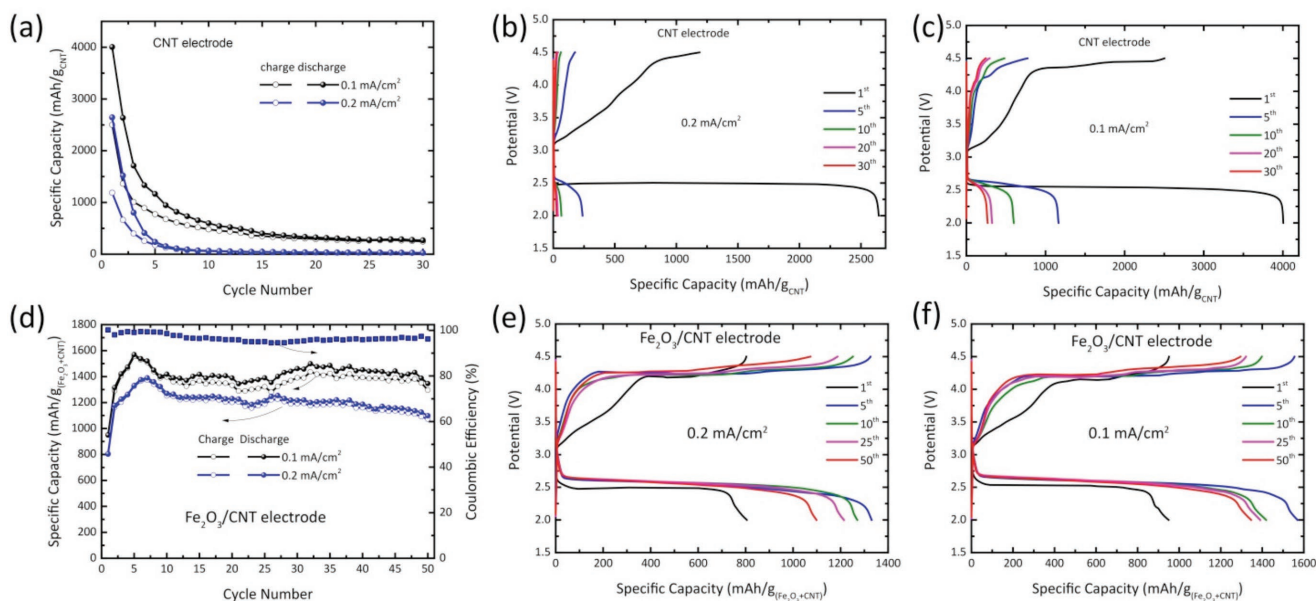


**Figure 1.** Cycling performance of a) CNT and d)  $\text{Fe}_2\text{O}_3/\text{CNT}$  oxygen cathodes during deep (dis)charge by employing a potential window of 2.0–4.5 V, measured in 0.5 M LiTFSI/TEGDME electrolyte at current densities of 0.1 and 0.2  $\text{mA cm}^{-2}$ , respectively in  $\text{Li}-\text{O}_2$  batteries at 1.0 bar  $\text{O}_2$  pressure. b,c,e,f) selected, potential cutoff, galvanostatic (dis)charge profiles for CNT and  $\text{Fe}_2\text{O}_3/\text{CNT}$  oxygen cathodes, respectively.

As an anode in lithium-ion batteries,  $\text{Fe}_2\text{O}_3$  nanostructured materials follow a series of Li-insertion processes resulting in two voltage plateaus at  $\approx 1.2$  and 0.75 V, respectively.<sup>[51,52]</sup> A  $\text{Fe}_2\text{O}_3/\text{CNT}$  electrode cycled in Ar within a 2.0–4.5 V window (Figure S4, Supporting Information) shows a reversible capacity of only 24  $\text{mA h g}^{-1}$  ( $0.027 \text{ mA h cm}^{-2}$ ) at a current density of 0.1  $\text{mA cm}^{-2}$ . On the other hand, in the presence of  $\text{O}_2$ , the  $\text{Fe}_2\text{O}_3/\text{CNT}$  cathode displays a stable discharge plateau at around 2.6 V, as shown in Figure 1e,f. Thus, within the potential window of 2.0–4.0 V, the Li-intercalation reaction does not contribute to the discharge capacity of the  $\text{Fe}_2\text{O}_3/\text{CNT}$  cathode in a  $\text{Li}-\text{O}_2$  battery.

Figure S5 (Supporting Information) shows the cyclic voltammetry curves of CNT and  $\text{Fe}_2\text{O}_3/\text{CNT}$  cathodes, respectively. The observed bell shaped oxygen reduction curves of both the CNT and  $\text{Fe}_2\text{O}_3/\text{CNT}$  cathodes represent the expected formation of  $\text{Li}_2\text{O}_2$ .<sup>[53]</sup> Due to the low electronic conductivity of lithium oxide, the oxidation overpotential is expected to be high. The oxygen evolution anodic peaks can be attributed to the oxidation of  $\text{Li}_2\text{O}_2$ .<sup>[53,54]</sup>

## 2.2. Analysis of the Evolution of Products During (Dis)charge

In principle, the potential of a  $\text{Li}-\text{O}_2$  battery system should sharply increase when the discharge product is completely decomposed during charge. This is typically observed in Li-ion battery electrodes, where after all of the removable lithium ions are extracted, the potential steeply increases toward the cutoff voltage. However, this phenomenon is seldom reported for  $\text{Li}-\text{O}_2$  batteries, where capacity restriction is typically used to demonstrate the electrochemical performance of oxygen cathodes. Thereby, side reactions with the electrolyte that occur at large and small potentials are avoided, at the same time the

reversibility is artificially improved as the battery is only partially discharged. Potential limited cycling utilizes the full capacity, and is more challenging, because side reactions are unavoidable in an aprotic  $\text{Li}-\text{O}_2$  battery at high charge potentials. These parasitic reactions lead to the formation of  $\text{Li}_2\text{CO}_3$ , the decomposition of the electrolyte, and the decomposition of the binder in the cathode.<sup>[55]</sup>

To investigate the reversibility of the products on the  $\text{Fe}_2\text{O}_3/\text{CNT}$  oxygen cathodes at high charge potentials, the discharge capacity was restricted to 0.5 and 0.25 mA h and the  $\text{Li}-\text{O}_2$  batteries were subsequently charged to 4.5 V at current densities of 0.1 and 0.2  $\text{mA cm}^{-2}$ , respectively, as shown in Figure S6 (Supporting Information). Under these conditions the  $\text{Li}-\text{O}_2$  battery also exhibits stable cycling, where the potential limited charge capacity is very close to the discharge capacity over 50 cycles (Figure S6a,d). The discharge plateau is close to 2.6 V (Figure S6b–f). Notably, the charge voltage increases to 4.5 V at the end of the charge process following the stable charge plateaus, which is rarely reported for  $\text{Li}-\text{O}_2$  battery (dis)charge profiles. From the ex situ X-ray powder diffraction (XRD) patterns shown in Figure S7a (Supporting Information), it is difficult to observe differences between the diffraction peaks of the pristine and discharged  $\text{Fe}_2\text{O}_3/\text{CNT}$  cathode at the current densities of 0.1 and 0.2  $\text{mA cm}^{-2}$ , as expected owing to the similar lattice spacing of (104)  $\text{Fe}_2\text{O}_3$  and (100)  $\text{Li}_2\text{O}_2$  planes (Figure S1, Supporting Information). The scanning electron microscopy (SEM) images also show no significant difference between the pristine sample (Figure S7b, Supporting Information) and the discharged cathode (Figure S7c, Supporting Information), with the exception of a film-like structure that forms at a current density of 0.2  $\text{mA cm}^{-2}$ . This most likely represents the deposition of a quasi-amorphous thin  $\text{Li}_2\text{O}_2$  film, which is known to occur at high (dis)charge currents.<sup>[8]</sup> Using the titration experiment developed by McCloskey and co-workers<sup>[56]</sup> (Figure S8,

Supporting Information), the yield of  $\text{Li}_2\text{O}_2$  after first discharge to 2.0 V on the surface of  $\text{Fe}_2\text{O}_3/\text{CNT}$  cathodes was found to be 95.7% and 96.5% compared to the theoretical capacity at the current density of 0.2 and 0.1  $\text{mA cm}^{-2}$ , respectively, confirming that the discharge capacity from the  $\text{Fe}_2\text{O}_3/\text{CNT}$  cathode is mainly due to the formation of  $\text{Li}_2\text{O}_2$ . Online electrochemical mass spectrometry (OEMS) measurements were performed to quantify the  $\text{O}_2$  evolution during charge (Figure S9, Supporting Information). Even though  $\text{O}_2$  evolution does not match the number of electrons involved in the first charge in the OEMS experiment, only  $\text{O}_2$  is detected over the charge plateau (Figure S9a, Supporting Information). At the end of charge,  $\text{CO}_2$  is generated from the decomposition of some carbonates that are unavoidably generated via reaction of superoxide and/or peroxide with the electrolyte. This is the reason for the lower  $e^-/\text{O}_2$  ratio in Figure S9b (Supporting Information) (compared to the theoretical value of  $2e^-/\text{O}_2$  corresponding to pure  $\text{O}_2$  evolution); namely, some byproducts form that are not related to the evolution of  $\text{O}_2$ . Unfortunately, despite the increased columbic efficiency, the stability of all the cell components (electrolyte, CNT conductive support, etc.) in the electrolyte with an intermediate donor number still needs to be addressed in order to obtain a ratio of 2.0  $e^-/\text{O}_2$ . However, the aim of this study is to show the beneficial impact of the  $\text{Fe}_2\text{O}_3$  on the reversible growth of  $\text{Li}_2\text{O}_2$ , resulting in the improved cycling under potential limited cycling.

To verify the formation and decomposition of  $\text{Li}_2\text{O}_2$  on the  $\text{Fe}_2\text{O}_3/\text{CNT}$  cathode, operando XRD was carried out on a  $\text{Li}-\text{O}_2$  battery cycled within a potential window of 2.0–4.5 V at a current density of 0.2  $\text{mA cm}^{-2}$  in a 0.5 M LiTFSI/TEGDME electrolyte (Figure 2). Since the (104) and (110) lattice plane distances of  $\text{Fe}_2\text{O}_3$  are very similar to the (100)

and (101) planes of  $\text{Li}_2\text{O}_2$ , respectively (Figure S1, Supporting Information), the reflections are indistinguishable in ex situ XRD measurements of discharged cathodes, especially due to the broadening of nanosized  $\text{Fe}_2\text{O}_3$  peaks. However, the 2D contour operando XRD patterns in the  $2\theta$  region of  $31.5\text{--}37^\circ$  (Figure 2) show a symmetric broadening of the (100)/(104) and the (101)/(110)  $\text{Li}_2\text{O}_2/\text{Fe}_2\text{O}_3$  lattice planes, confirming the gradual formation and decomposition of  $\text{Li}_2\text{O}_2$ .

To further investigate the discharge product formed on the cathode surface at a current density of 0.2  $\text{mA cm}^{-2}$ , ex situ X-ray photoelectron spectroscopy (XPS) analysis (Figure 3) was carried out on the pristine  $\text{Fe}_2\text{O}_3/\text{CNT}$  cathode and cathodes from discharged and recharged batteries (discharge to 2.0 V and recharge to 4.5 V; the electrochemical performance of these batteries is shown in Figure S10 in the Supporting Information). All spectra were calibrated using the C1s peak of CNT at 284.48 eV. The survey scan from 0 to 800 eV is given in Figure 3a and shows the relative change in the quantities of oxygen, lithium, and iron on the surface of the  $\text{Fe}_2\text{O}_3/\text{CNT}$  cathodes. The relative intensity of the Fe2p peaks for the  $\text{Fe}_2\text{O}_3/\text{CNT}$  cathodes diminishes after the first and fifth discharge (black and blue lines in Figure 3a), but recovers after recharge (red line in Figure 3a), indicating that the surface of the cathode is covered with a discharge product which is removed after charge. Figure 3b–d displays the XPS spectra in the Fe2p, O1s, and Li1s/Fe3p regions, respectively. The Fe2p region from 705 to 730 eV shows the characteristic  $2p_{1/2}$  and  $2p_{3/2}$  doublet which is attributed to  $\text{Fe}_2\text{O}_3$  (pink line in Figure 3b).<sup>[57]</sup> After the first discharge, the peak becomes less prominent (black line in Figure 3b), and after the fifth discharge the peak becomes indistinguishable (blue line in Figure 3b). However, when the cathode is recharged to 4.5 V, the Fe2p signal completely reappears, and is similar to the pristine sample (red and pink lines in Figure 3b). This is an indication of the formation and decomposition of products on the cathode surface during (dis)charge. In addition, after first discharge, the main peak of Fe2p slightly shifts to low binding energy compared to the pristine and recharged cathodes, which may be attributed to the surface redox activities (involving  $\text{Fe}^{2+/3+}$  redox couple). Further, this could probably overlap with the surface bonds between  $\text{Li}_2\text{O}_2$  and  $\text{Fe}_2\text{O}_3$ . In the pristine electrode, O1s spectral peaks (pink line in Figure 3c) appear from 528 to 533 eV and can be assigned to Fe–O and Fe–OH from  $\text{Fe}_2\text{O}_3$ .<sup>[57]</sup> The features (pink line in Figure 3d) in the region from 55.5 to 57.3 eV can be attributed to the Fe3p contribution from  $\text{Fe}_2\text{O}_3$ . It is interesting to note that after the first and fifth discharge to 2.0 V, the spectral peaks in the O1s and Fe3p/Li1s regions (black and blue lines in Figure 3c,d) shift to binding energies of 54.6 and 531.2 eV, mainly corresponding to the lithium and oxygen contributions from

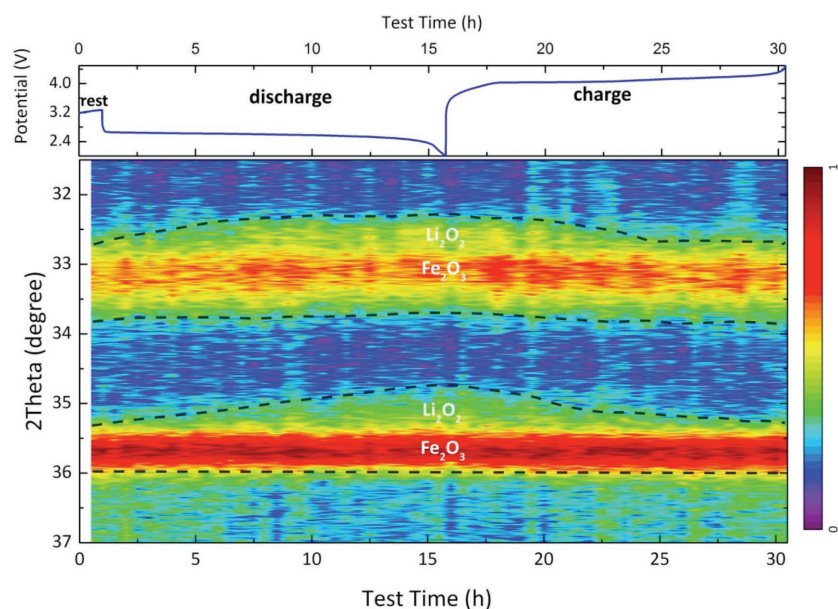


**Figure 2.** Top: (Dis)charge profile of the  $\text{Fe}_2\text{O}_3/\text{CNT}$  oxygen cathode in an operando  $\text{Li}-\text{O}_2$  battery. Bottom: 2D contour plots of the operando XRD patterns showing the  $2\theta$  region between  $31.5\text{--}37^\circ$  during a complete (dis)charge cycle, demonstrating the formation of  $\text{Li}_2\text{O}_2$  and its decomposition. The battery was (dis)charged using a 0.5 M LiTFSI/TEGDME electrolyte within a potential window of 2.0–4.5 V at a current density of 0.2  $\text{mA cm}^{-2}$ .

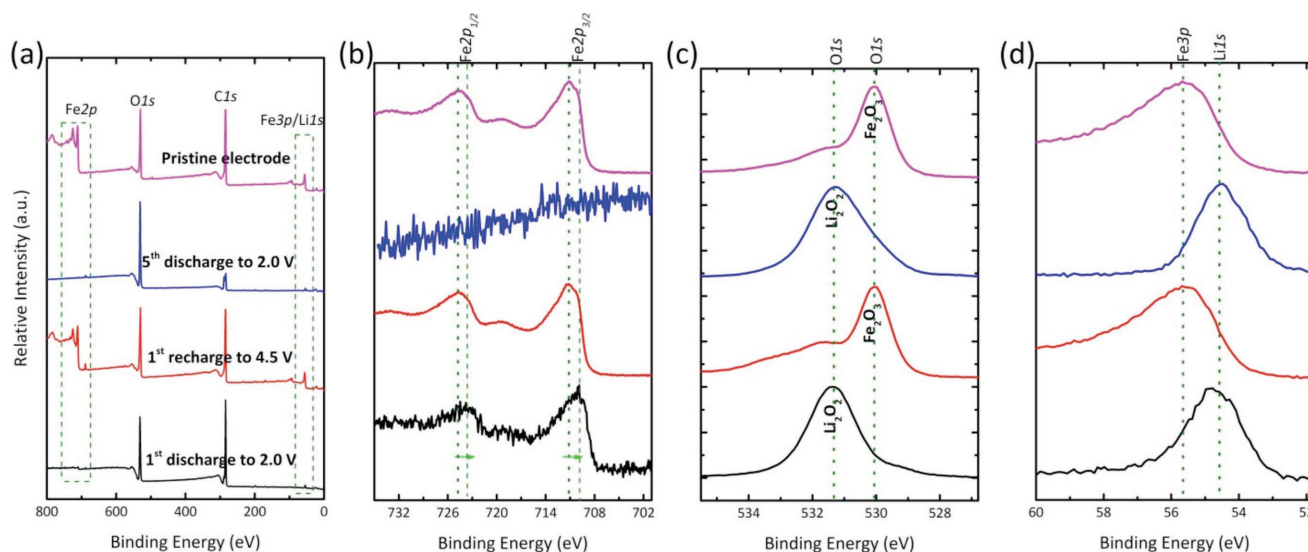


**Figure 3.** a) XPS survey scans of  $\text{Fe}_2\text{O}_3/\text{CNT}$  oxygen cathodes at different (dis)charge states. b,c,d) High resolution XPS in the Fe2p, O1s, and Li1s or Fe3p regions, respectively for the  $\text{Fe}_2\text{O}_3/\text{CNT}$  oxygen cathode at different states of (dis)charge. The black, red, blue, and pink lines represent the cathode at the state of first discharge to 2.0 V, first recharge to 4.5 V, fifth discharge to 2.0 V, and pristine states, respectively.

$\text{Li}_2\text{O}_2$ , respectively.<sup>[58]</sup> Furthermore, after recharge (red line in Figure 3c,d), the shift of peaks in this region returns to their original positions, indicating reappearance of the Fe2p and Fe3p contributions and hence the removal of  $\text{Li}_2\text{O}_2$  from the cathode surface. In summary, from the XPS analysis of the pristine, discharged and recharged samples, we conclude that  $\text{Li}_2\text{O}_2$  is the main product formed reversibly on the  $\text{Fe}_2\text{O}_3/\text{CNT}$  cathode surface during (dis)charge in the Li– $\text{O}_2$  battery.

**Figure 4** shows the 2D contour plot of the operando XRD patterns of the  $\text{Fe}_2\text{O}_3/\text{CNT}$  cathode at a lower current density of  $0.05 \text{ mA cm}^{-2}$  compared to that shown in Figure 2. Discernable  $\text{Li}_2\text{O}_2$  XRD peaks are observed on the  $\text{Fe}_2\text{O}_3/\text{CNT}$  cathode when the discharge current density is lowered to  $0.05 \text{ mA cm}^{-2}$  (**Figure 5a**). The gradual increase and decrease in the intensities of the  $\text{Li}_2\text{O}_2$  reflections, corresponding to the (100) and (101) planes of  $\text{Li}_2\text{O}_2$  (**Figure 4**), indicate the gradual formation and decomposition of  $\text{Li}_2\text{O}_2$  on the  $\text{Fe}_2\text{O}_3/\text{CNT}$  cathode as a function of (dis)charge time. The ex situ SEM image of the  $\text{Fe}_2\text{O}_3/\text{CNT}$  cathode after discharge to 2.0 V shows a homogenous platelet morphology of the  $\text{Li}_2\text{O}_2$  particles (**Figure 5b**). Based on the Rietveld refinement of the sequential operando XRD patterns (**Figure 5c**), we obtained the average coherent size of  $\text{Li}_2\text{O}_2$  as a function of (dis)charge time (**Figure 5d**). During the refinement, the  $\text{Fe}_2\text{O}_3$  parameters were fixed based on the refinement result as shown in **Figure S11** (Supporting Information). The average coherent length of the  $\text{Li}_2\text{O}_2$  crystallite platelets first increases during initial discharge, after which it decreases as discharge progresses. This indicates the formation of larger and more anisotropic shaped  $\text{Li}_2\text{O}_2$  crystallites at the initial stages of discharge. The deposition of smaller and more isotropic  $\text{Li}_2\text{O}_2$  occurs as discharge progresses, similar to what we reported previously.<sup>[59]</sup> During charge, smaller  $\text{Li}_2\text{O}_2$  crystallites preferentially decompose followed by the decomposition of the larger  $\text{Li}_2\text{O}_2$  crystallites, as can be concluded from the initial increase in the average coherence length of  $\text{Li}_2\text{O}_2$  (after which it remains constant to the end of charge).<sup>[60]</sup>

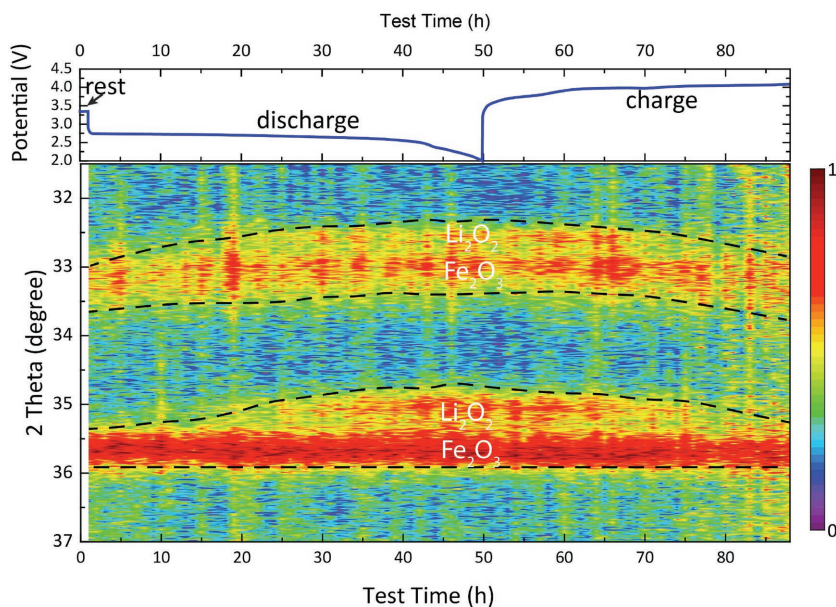


**Figure 4.** Top: (Dis)charge profile of the electrochemical performance of the  $\text{Fe}_2\text{O}_3/\text{CNT}$  oxygen cathode in an operando Li– $\text{O}_2$  battery. Bottom: 2D contour plots of the operando XRD patterns showing the  $2\theta$  region between  $31.5\text{--}37^\circ$ , during a complete (dis)charge cycle demonstrating the formation and decomposition of  $\text{Li}_2\text{O}_2$ . The operando Li– $\text{O}_2$  battery was (dis)charged using a  $0.5 \text{ M LiTFSI/TEGDME}$  electrolyte within a potential window of 2.0–4.5 V at a current density of  $0.05 \text{ mA cm}^{-2}$ .

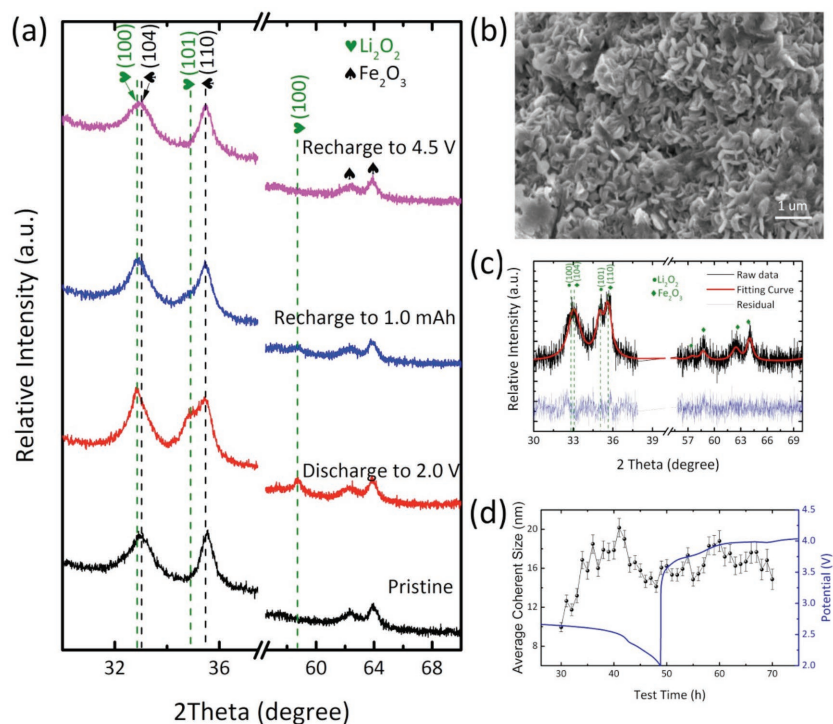


**Figure 5.** a) Ex situ XRD patterns of the  $\text{Fe}_2\text{O}_3/\text{CNT}$  cathode at different discharge and recharge states. b) SEM image of the  $\text{Li}_2\text{O}_2$  particles formed on the  $\text{Fe}_2\text{O}_3/\text{CNT}$  cathode at the end of discharge. c) Rietveld refinement result of the XRD patterns. d) Average coherent size of  $\text{Li}_2\text{O}_2$  obtained from Rietveld refinement as a function of (dis)charge time. The corresponding voltage profile measured during (dis)charge is illustrated in the graph.

**Figure 6** displays XRD patterns and SEM images of the discharge product formed on the cathode surface at even lower current densities ( $0.02 \text{ mA cm}^{-2}$ ). Very evident  $\text{Li}_2\text{O}_2$  peaks are observed in the XRD patterns of both the discharged CNT and  $\text{Fe}_2\text{O}_3/\text{CNT}$  cathodes, as shown in Figure 6a. After complete discharge at a current density of  $0.02 \text{ mA cm}^{-2}$ , the surface of the CNT cathode (Figure 6b,c) shows homogenous toroidal  $\text{Li}_2\text{O}_2$  particles—about 500 nm in diameter and 100 nm in thickness, randomly oriented on the cathodes. In contrast, the surface of the  $\text{Fe}_2\text{O}_3/\text{CNT}$  cathode (Figure 6d,e) at the end of

### 3. Mechanism

Since TEGDME has an intermediate DN,  $\text{Li}_2\text{O}_2$  formation is expected to take place both via formation in the solvent and directly on the surface of the cathode.<sup>[5,6]</sup> The different  $\text{Li}_2\text{O}_2$  morphology obtained upon adding  $\text{Fe}_2\text{O}_3$  to the CNT cathodes, observed in the SEM images in Figure 6b–e, demonstrates that the presence of  $\text{Fe}_2\text{O}_3$  influences the growth mechanism of the  $\text{Li}_2\text{O}_2$  particles. In this context, we remind that  $\text{Fe}_2\text{O}_3$  is a wide band gap hopping semiconductor, but the presence of extensive

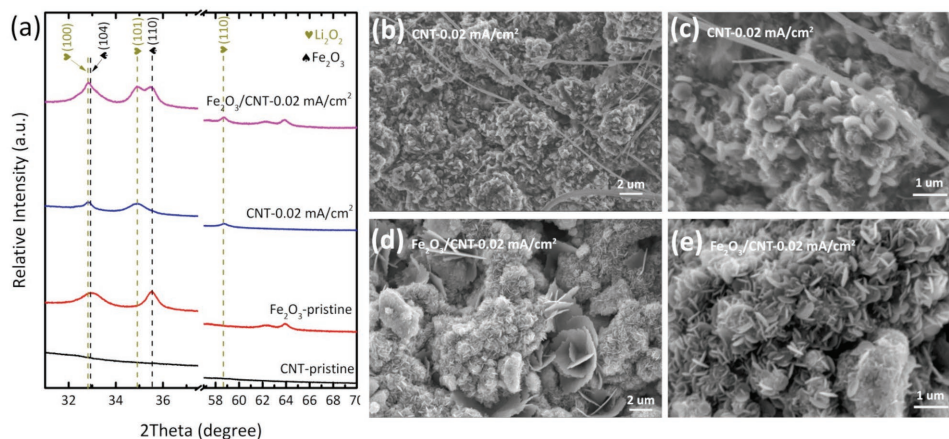


**Figure 6.** a) The  $\text{Li}_2\text{O}_2$  and  $\text{Fe}_2\text{O}_3$  XRD reflections resulting from CNT and  $\text{Fe}_2\text{O}_3/\text{CNT}$  oxygen cathodes at the end of complete discharge, respectively. b, c) and d, e) SEM images of the CNT cathode and the  $\text{Fe}_2\text{O}_3/\text{CNT}$  cathode at the end of discharge at a current density of  $0.02 \text{ mA cm}^{-2}$ .

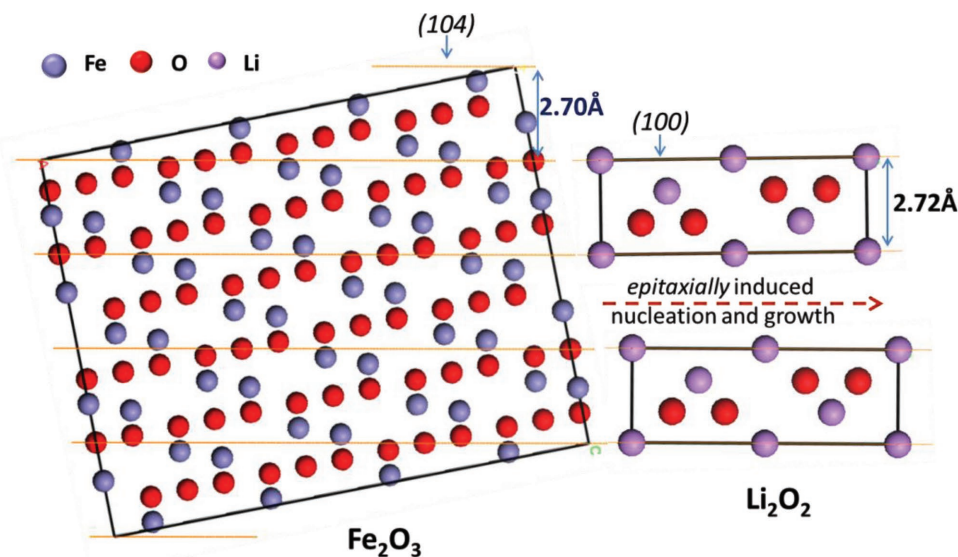


**Figure 7.** Schematic of the proposed “epitaxially induced nucleation and growth” mechanism of  $\text{Li}_2\text{O}_2$  on  $\text{Fe}_2\text{O}_3$ . The  $\text{Fe}_2\text{O}_3$  crystallites expose the (104) lattice spacing at their surface, which matches the (100) lattice distance of the  $\text{Li}_2\text{O}_2$  crystallites, which grow in the (001) direction perpendicular to the  $\text{Fe}_2\text{O}_3$  surface.

defects leads to significant electronic conductivity. Previously, hexagonal NiO nanoparticles were used as nanoseed crystals to induce equiaxial growth of  $\text{Li}_2\text{O}_2$  owing to their similar *a*- and *b*-lattice parameters.<sup>[30]</sup> The  $\text{Fe}_2\text{O}_3$  nanoseed particles have even more similar interplanar spacing to that of  $\text{Li}_2\text{O}_2$ , as shown in **Figure 7** and Figure S1 (Supporting Information). In the XRD pattern of the  $\text{Fe}_2\text{O}_3$  nanoparticles, the (104) reflection is broader than the (110) reflection (Figure S11, Supporting Information), reflecting the anisotropic shape of the  $\text{Fe}_2\text{O}_3$  nanoparticles.<sup>[58]</sup> High resolution transmission electron microscopy (HRTEM) image (Figure S14, Supporting Information) indicates that the  $\text{Fe}_2\text{O}_3$  nanoparticles have a 2D shape, where the long-dimension is along the [hk0] direction and the short-dimension is along the [00l] direction. TEM image also shows that the interplanar spacing on the surface of the  $\text{Fe}_2\text{O}_3$  crystallites is close to 0.27 nm. The similar value of the d-spacing of the  $\text{Li}_2\text{O}_2$  (100) lattice planes (0.272 nm in Figure S1 in the Supporting Information) led us to hypothesize a “epitaxially induced nucleation and growth” mechanism for  $\text{Li}_2\text{O}_2$  growth on  $\text{Fe}_2\text{O}_3$ . This mechanism is schematically shown in Figure 7 where (1) the  $\text{Li}_2\text{O}_2$  crystallite nucleates on the [0k0] surface facets of the  $\text{Fe}_2\text{O}_3$  crystallite; (2) because the dominant  $\text{Li}_2\text{O}_2$  growth direction is (001),<sup>[60,61]</sup> and the footprint of the  $\text{Li}_2\text{O}_2$  crystallite is in the (100)/(010) direction, which matches on the (104) lattice plane exposed on the  $\text{Fe}_2\text{O}_3$  surface. This is consistent with the disc-like  $\text{Li}_2\text{O}_2$  particles that appear to grow perpendicular to the  $\text{Fe}_2\text{O}_3/\text{CNT}$  electrode surface observed in Figure 6d,e. The Rietveld refinement shows no significant change in lattice parameters of the  $\text{Li}_2\text{O}_2$  that forms on the CNT and  $\text{Fe}_2\text{O}_3/\text{CNT}$  cathodes (Figure S13 and Table S1, Supporting Information) in contrast to NiO.<sup>[30]</sup>

It is established that the current density affects the morphology of the  $\text{Li}_2\text{O}_2$  formed.<sup>[8]</sup> This is also confirmed by the present XRD studies where the average coherent length of  $\text{Li}_2\text{O}_2$  at relatively low current density ( $0.02 \text{ mA cm}^{-2}$ ) (Table S1, Supporting Information) is larger than that at high current

density ( $0.05 \text{ mA cm}^{-2}$ ) (Figure 5d) on the  $\text{Fe}_2\text{O}_3/\text{CNT}$  electrode. Interestingly, comparing the XRD refinement results (Table S1, Supporting Information) of the average coherent length of  $\text{Li}_2\text{O}_2$  crystallites, the larger and much more isotropic  $\text{Li}_2\text{O}_2$  crystallites are formed on the  $\text{Fe}_2\text{O}_3/\text{CNT}$  cathodes compared to that on CNT cathode. However, comparing the SEM images in Figures 5b and 6b,e suggests that significantly smaller disc-like  $\text{Li}_2\text{O}_2$  secondary particles form on  $\text{Fe}_2\text{O}_3/\text{CNT}$  cathodes. The smaller secondary particles will be easier to decompose upon charge due to their relatively higher surface area. Another aspect of the proposed epitaxial growth mechanism is that the larger crystallites indicate that the  $\text{Fe}_2\text{O}_3$  enhances the crystallinity of the  $\text{Li}_2\text{O}_2$ , thus suppressing the formation of passivating amorphous films, as also observed on NiO seed crystallites,<sup>[30]</sup> and enhances reversibility of  $\text{Li}_2\text{O}_2$ . This is particularly noteworthy as the local current density is most likely much larger on the  $\text{Fe}_2\text{O}_3/\text{CNT}$  cathodes because of their smaller surface area. Another advantage is that at high charge potentials the  $\text{Li}_2\text{O}_2\text{-Fe}_2\text{O}_3$  interface can be expected to be more stable than  $\text{Li}_2\text{O}_2\text{-carbon}$  interface, which forms a thin isolating  $\text{Li}_2\text{CO}_3$  film.<sup>[10]</sup> In this context, it is important to note that hematite  $\text{Fe}_2\text{O}_3$  nanostructures exhibit good electronic conductivity,<sup>[50,62,63]</sup> necessary for the electron transport between the carbon matrix and the  $\text{Li}_2\text{O}_2$ . Finally, preferential adsorption of oxygen onto the surface of  $\alpha\text{-Fe}_2\text{O}_3$  surface<sup>[64]</sup> may promote the deposition of  $\text{Li}_2\text{O}_2$  on the  $\text{Fe}_2\text{O}_3$  surface.

These favorable properties of  $\alpha\text{-Fe}_2\text{O}_3$  most likely contributing to the reversible growth of  $\text{Li}_2\text{O}_2$  provide a rationale for the improved reversibility upon potential-limited cycling of the  $\text{Fe}_2\text{O}_3/\text{CNT}$  cathodes in direct comparison to the CNT cathodes. As discussed, the  $\text{Fe}_2\text{O}_3$  impacts the reversible formation of  $\text{Li}_2\text{O}_2$ , which appears to be the origin of the improved reversibility; however, this is not expected to prevent detrimental reactions between the intermediate discharge products and the electrolyte. The relatively large coulombic

efficiency ( $\approx >95\%$  for  $\text{Li}_2\text{O}_2$  production), especially under potential limited cycling conditions, in combination with the titration results suggests a reduction in the degree of side reactions. Possibly, faster  $\text{Li}_2\text{O}_2$  nucleation induced by  $\text{Fe}_2\text{O}_3$  may reduce the exposure time of intermediate discharge products. However, the far from theoretical  $\text{O}_2$  evolution measured by OEMS indicates that parasitic reactions as generally observed for this system or reversible reactions that do not involve  $\text{O}_2$  evolution cannot be excluded, which will be topic for further investigations.

## 4. Conclusions

In conclusion, we have demonstrated that a  $\text{Li}-\text{O}_2$  battery consisting of an  $\text{Fe}_2\text{O}_3/\text{CNT}$  oxygen cathode with TEGDME electrolyte offers more reversible cycling on deep potential-restricted (dis)charge with a capacity retention of  $\approx 1098 \text{ mA h g}^{-1}$  ( $0.95 \text{ mA h cm}^{-2}$ ) after 50 cycles at a current density of  $0.2 \text{ mA cm}^{-2}$ . Operando XRD and ex situ XPS measurements reveal the reversible formation and decomposition of  $\text{Li}_2\text{O}_2$  crystallites during (dis)charge at high and intermediate current densities ( $0.2$  and  $0.05 \text{ mA cm}^{-2}$ ). At low current densities ( $0.02 \text{ mA cm}^{-2}$ ) small disc-like particles and some large plates of  $\text{Li}_2\text{O}_2$  form perpendicular to the  $\text{Fe}_2\text{O}_3/\text{CNT}$  electrode surface, which are very different from that of toroidal  $\text{Li}_2\text{O}_2$  particles formed on the CNT electrode. Based on the similar lattice spacing of the (104)/(100) reflections in  $\text{Fe}_2\text{O}_3/\text{Li}_2\text{O}_2$ , we have hypothesized a “epitaxially induced nucleation and growth” mechanism. The resulting  $\text{Li}_2\text{O}_2$  has a more isotropic crystallite shape and a smaller secondary particle size, where the epitaxial growth and the larger surface area appear to be responsible for the improved reversibility of the  $\text{Li}_2\text{O}_2$  formation and oxidation. Although electrolyte stability remains a critical issue, the “epitaxially induced nucleation and growth” mechanism proposed in this work can be potentially used to gain control over the  $\text{Li}_2\text{O}_2$  growth and thereby improve the electrochemical performance of  $\text{Li}-\text{O}_2$  batteries.

## Supporting Information

Supporting Information is available from the Wiley Online Library or from the author.

## Acknowledgements

The authors thank Kees Goubitz, Michel Steenvoorden, and Frans Ooms for their assistance with experiments. The authors greatly acknowledge financial support from the China Scholarship Council (CSC), the grants (National Natural Science Foundation of China (51472189)) from Q.Z. The research leading to these results has received funding from the European Research Council under the European Union’s Seventh Framework Program (FP/2007-2013)/ERC Grant Agreement no. [307161] of M.W. L.N. gratefully acknowledges NSERC for financial support. FlexBatteries (grant agreement no.704659) from Marie Skłodowska-Curie action is also acknowledged.

## Conflict of Interest

The authors declare no conflict of interest.

## Keywords

aprotic  $\text{Li}-\text{O}_2$  batteries, deep (dis)charge, epitaxial growth mechanism,  $\text{Fe}_2\text{O}_3$  seed catalysts

Received: December 13, 2017

Revised: January 31, 2018

Published online:

- [1] D. Aurbach, B. D. McCloskey, L. F. Nazar, P. G. Bruce, *Nat. Energy* **2016**, *1*, 16128.
- [2] A. C. Luntz, B. D. McCloskey, *Chem. Rev.* **2014**, *114*, 11721.
- [3] J. Lu, L. Li, J.-B. Park, Y.-K. Sun, F. Wu, K. Amine, *Chem. Rev.* **2014**, *114*, 5611.
- [4] R. Black, B. Adams, L. F. Nazar, *Adv. Energy Mater.* **2012**, *2*, 801.
- [5] L. Johnson, C. Li, Z. Liu, Y. Chen, S. A. Freunberger, P. C. Ashok, B. B. Praveen, K. Dholakia, J. M. Tarascon, P. G. Bruce, *Nat. Chem.* **2014**, *6*, 1091.
- [6] N. B. Aetukuri, B. D. McCloskey, J. M. García, L. E. Krupp, V. Viswanathan, A. C. Luntz, *Nat. Chem.* **2015**, *7*, 50.
- [7] C. M. Burke, V. Pande, A. Khetan, V. Viswanathan, B. D. McCloskey, *Proc. Natl. Acad. Sci. USA* **2015**, *112*, 9293.
- [8] B. D. Adams, C. Radtke, R. Black, M. L. Trudeau, K. Zaghbi, L. F. Nazar, *Energy Environ. Sci.* **2013**, *6*, 1772.
- [9] B. D. McCloskey, R. Scheffler, A. Speidel, G. Girishkumar, A. C. Luntz, *J. Phys. Chem. C* **2012**, *116*, 23897.
- [10] B. D. McCloskey, A. Speidel, R. Scheffler, D. C. Miller, V. Viswanathan, J. S. Hummelshøj, J. K. Nørskov, A. C. Luntz, *J. Phys. Chem. Lett.* **2012**, *3*, 997.
- [11] Y.-C. Lu, Z. Xu, H. A. Gasteiger, S. Chen, K. Hamad-Schifferli, Y. Shao-Horn, *J. Am. Chem. Soc.* **2010**, *132*, 12170.
- [12] Y.-C. Lu, H. A. Gasteiger, Y. Shao-Horn, *J. Am. Chem. Soc.* **2011**, *133*, 19048.
- [13] B. D. McCloskey, R. Scheffler, A. Speidel, D. S. Bethune, R. M. Shelby, A. C. Luntz, *J. Am. Chem. Soc.* **2011**, *133*, 18038.
- [14] Z. Peng, S. A. Freunberger, Y. Chen, P. G. Bruce, *Science* **2012**, *337*, 563.
- [15] H. D. Lim, H. Song, H. Gwon, K.-Y. Park, J. Kim, Y. Bae, H. Kim, S.-K. Jung, T. Kim, Y. H. Kim, X. Lepro, R. Ovalle-Robles, R. H. Baughman, K. Kang, *Energy Environ. Sci.* **2013**, *6*, 3570.
- [16] E. Yilmaz, C. Yogi, K. Yamanaka, T. Ohta, H. R. Byon, *Nano Lett.* **2013**, *13*, 4679.
- [17] Z. Jian, P. Liu, F. Li, P. He, X. Guo, M. Chen, H. Zhou, *Angew. Chem., Int. Ed.* **2014**, *53*, 442.
- [18] Li, F.; Y. Chen, D.-M. Tang, Z. Jian, C. Liu, D. Golberg, A. Yamada, H. Zhou, *Energy Environ. Sci.* **2014**, *7*, 1648.
- [19] S. Ma, Y. Wu, J. Wang, Y. Zhang, Y. Zhang, X. Yan, Y. Wei, P. Liu, J. Wang, K. Jiang, S. Fan, Y. Xu, Z. Peng, *Nano Lett.* **2015**, *15*, 8084.
- [20] D. W. Su, S. X. Dou, G. X. Wang, *J. Mater. Chem. A* **2015**, *3*, 18384.
- [21] S. Tong, M. Zheng, Y. Lu, Z. Lin, X. Zhang, P. He, H. Zhou, *Chem. Commun.* **2015**, *51*, 7302.
- [22] F. Jiao, P. G. Bruce, *Adv. Mater.* **2007**, *19*, 657.
- [23] A. Débart, A. J. Paterson, J. Bao, P. G. Bruce, *Angew. Chem.* **2008**, *120*, 4597.
- [24] J. Wu, H. W. Park, A. Yu, D. Higgins, Z. Chen, *J. Phys. Chem. C* **2012**, *116*, 9427.

- [25] R. Black, J.-H. Lee, B. Adams, C. A. Mims, L. F. Nazar, *Angew. Chem., Int. Ed.* **2013**, *52*, 392.
- [26] W.-H. Ryu, T.-H. Yoon, S. H. Song, S. Jeon, Y.-J. Park, I.-D. Kim, *Nano Lett.* **2013**, *13*, 4190.
- [27] G. Zhao, R. Mo, B. Wang, L. Zhang, K. Sun, *Chem. Mater.* **2014**, *26*, 2551.
- [28] R. Gao, J. Zhu, X. Xiao, Z. Hu, J. Liu, X. J. Liu, *Phys. Chem. C* **2015**, *119*, 4516.
- [29] M. A. Schroeder, A. J. Pearse, A. C. Kozen, X. Chen, K. Gregorczyk, X. Han, A. Cao, L. Hu, S. B. Lee, G. W. Rubloff, M. Noked, *Chem. Mater.* **2015**, *27*, 5305.
- [30] S. Ganapathy, Z. Li, M. S. Anastasaki, S. Basak, X.-F. Miao, K. Goubitz, H. W. Zandbergen, F. M. Mulder, M. Wagemaker, *J. Phys. Chem. C* **2016**, *120*, 18421.
- [31] K. R. Yoon, G. Y. Lee, G. J.-W. Jung, N.-H. Kim, S. O. Kim, I.-D. Kim, *Nano Lett.* **2016**, *16*, 2076.
- [32] P. Zhang, R. Wang, M. He, J. Lang, S. Xu, X. Yan, *Adv. Funct. Mater.* **2016**, *26*, 1354.
- [33] P. Zhang, S. Zhang, M. He, J. Lang, A. Ren, S. Xu, X. Yan, *Adv. Sci.* **2017**, *4*, 1700172.
- [34] S. H. Oh, L. F. Nazar, *Adv. Energy Mater.* **2012**, *2*, 903.
- [35] H. Wang, Y. Yang, Y. Liang, G. Zheng, Y. Li, Y. Cui, H. Dai, *Energy Environ. Sci.* **2012**, *5*, 7931.
- [36] F. Li, R. Ohnishi, Y. Yamada, J. Kubota, K. Domen, A. Yamada, H. Zhou, *Chem. Commun.* **2013**, *49*, 1175.
- [37] M. M. Ottakam Thotiyl, S. A. Freunberger, Z. Peng, Y. Chen, Z. Liu, P. G. Bruce, *Nat. Mater.* **2013**, *12*, 1050.
- [38] J. Xie, X. Yao, I. P. Madden, D.-E. Jiang, L.-Y. Chou, C.-K. Tsung, D. Wang, *J. Am. Chem. Soc.* **2014**, *136*, 8903.
- [39] D. Kundu, R. Black; B. Adams; K. Harrison, K. Zavadil, L. F. Nazar, *J. Phys. Chem. Lett.* **2015**, *6*, 2252.
- [40] P. Sennu, M. Christy, V. Aravindan, Y.-G. Lee, K. S. Nahm, Y.-S. Lee, *Chem. Mater.* **2015**, *27*, 5726.
- [41] F. Li, D.-M. Tang, T. Zhang, K. Liao, P. He, D. Golberg, A. Yamada, H. Zhou, *Adv. Energy Mater.* **2015**, *5*, 1500294.
- [42] K. Liao, X. Wang, Y. Sun, D. Tang, M. Han, P. He, X. Jiang, T. Zhang, H. Zhou, *Energy Environ. Sci.* **2015**, *8*, 1992.
- [43] D. Kundu, R. Black, E. J. Berg, L. F. Nazar, *Energy Environ. Sci.* **2015**, *8*, 1292.
- [44] W. Zhang, Y. Zeng, C. Xu, H. Tan, W. Liu, J. Zhu, N. Xiao, H. H. Hng, J. Ma, H. E. Hoster, R. Yazami, Q. Yan, *RSC Adv.* **2012**, *2*, 8508.
- [45] Z. Zhang, G. Zhou, W. Chen, Y. Lai, J. Li, *ECS Electrochem. Lett.* **2013**, *3*, A8.
- [46] J. Lu, Y. Qin, P. Du, X. Luo, T. Wu, Y. Ren, J. Wen, D. J. Miller, J. T. Miller, K. Amine, *RSC Adv.* **2013**, *3*, 8276.
- [47] F. Wang, X. Wu, C. Shen, Z. Wen, *J. Solid State Electrochem.* **2016**, *20*, 1831.
- [48] K. Shimizu, L. Sepunaru, R. G. Compton, *Chem. Sci.* **2016**, *7*, 3364.
- [49] M. Sun, Y. Dong, G. Zhang, J. Qu, J. Li, *J. Mater. Chem. A* **2014**, *2*, 13635.
- [50] A. Gurlo, N. Bârsan, A. Oprea, M. Sahn, T. Sahn, U. Weimar, *Appl. Phys. Lett.* **2004**, *85*, 2280.
- [51] M. V. Reddy, T. Yu, C. H. Sow, Z. X. Shen, C. T. Lim, G. V. Subba Rao, B. V. R. Chowdari, *Adv. Funct. Mater.* **2007**, *17*, 2792.
- [52] S. Hao, B. Zhang, S. Ball, J. Wu, M. Srinivasan, Y. Huang, *J. Mater. Chem. A* **2016**, *4*, 16569.
- [53] I. Gunasekara, S. Mukerjee, E. J. Plichta, M. A. Hendrickson, K. M. Abraham, *J. Electrochem. Soc.* **2015**, *162*, A1055.
- [54] J. Han, X. Guo, Y. Ito, P. Liu, D. Hojo, T. Aida, A. Hirata, T. Fujita, T. Adschiri, H. Zhou, M. Chen, *Adv. Energy Mater.* **2016**, *6*, 1601933.
- [55] D. Geng, N. Ding, T. S. A. Hor, S. W. Chien, Z. Liu, D. Wu, X. Sun, Y. Zong, *Adv. Energy Mater.* **2016**, *6*, 1502164.
- [56] B. D. McCloskey, A. Valery, A. C. Luntz, S. R. Gowda, G. M. Wallraff, J. M. Garcia, T. Mori, L. E. Krupp, *J. Phys. Chem. Lett.* **2013**, *4*, 2989.
- [57] J. Baltrusaitis, D. M. Cwiertny, V. H. Grassian, *Phys. Chem. Chem. Phys.* **2007**, *9*, 5542.
- [58] K. P. C. Yao, D. G. Kwabi, R. A. Quinlan, A. N. Mansour, A. Grimaud, Y.-L. Lee, Y.-C. Lu, Y. Shao-Horn, *J. Electrochem. Soc.* **2013**, *160*, A824.
- [59] Z. Li, S. Ganapathy, Y. Xu, J. R. Heringa, Q. Zhu, W. Chen, M. Wagemaker, *Chem. Mater.* **2017**, *29*, 1577.
- [60] S. Ganapathy, B. D. Adams, G. Stenou, M. S. Anastasaki, K. Goubitz, X.-F. Miao, L. F. Nazar, M. Wagemaker, *J. Am. Chem. Soc.* **2014**, *136*, 16335.
- [61] M. D. Radin, J. F. Rodriguez, F. Tian, D. J. Siegel, *J. Am. Chem. Soc.* **2012**, *134*, 1093.
- [62] A. G. Tamirat, J. Rick, A. A. Dubale, W.-N. Su, B.-J. Hwang, *Nanoscale Horiz.* **2016**, *1*, 243.
- [63] A. G. B. Williams, M. M. Scherer, *Environ. Sci. Technol.* **2004**, *38*, 4782.
- [64] M. Dai, L. Zhao, H. Gao, P. Sun, F. Liu, S. Zhang, K. Shimanoe, N. Yamazoe, G. Lu, *ACS Appl. Mater. Interfaces* **2017**, *9*, 8919.